

Cosmic Ray Oriented Performance Studies for the JEM-EUSO First Level Trigger

G. Abdellaoui^{ah}, S. Abe^{fu}, A. Acheli^{aa}, J.H. Adams Jr.^{pd}, S. Ahmad^{cb},
A. Ahriche^{ae}, J.-N. Albert^{ca}, D. Allard^{cc}, G. Alonso^{md}, L. Anchordoqui^{pf},
V. Andreev^{pe}, A. Anzalone^{eh,en}, W. Aouimeur^{aa}, Y. Arai^{fw}, N. Arsene^{ja},
K. Asano^{fg}, R. Attallah^{ac}, H. Attoui^{aa}, M. Ave Pernas^{mc}, S. Bacholle^{cc},
M. Bakiri^{aa}, P. Baragatti^{eo}, P. Barrillon^{ca}, S. Bartocci^{eo}, T. Batschi^{ic},
J. Bayer^{dd}, R. Bechini^{el}, T. Belenguer^{mb}, R. Bellotti^{ea,eb}, A. Belov^{kc},
K. Belov^{pe}, B. Benadda^{ah}, K. Benmessai^{ag}, A.A. Berlind^{ph},
M. Bertaina^{ek,el,1}, P.L. Biermann^{db}, S. Biktemerova^{ka}, F. Bisconti^{db},
N. Blanc^{oa}, J. Błęcki^{id}, S. Blin-Bondil^{cb}, P. Bobik^{la}, M. Bogomilov^{ba},
M. Bonamente^{pd}, R. Boudaoud^{aa}, E. Bozzo^{ob}, M.S. Briggs^{pd}, A. Bruno^{eb},
K.S. Caballero^{he}, F. Cafagna^{ca}, D. Campana^{ef}, J.-N. Capdevielle^{cc},
F. Capel^{na}, A. Caramete^{ja}, L. Caramete^{ja}, P. Carlson^{na}, R. Caruso^{ec,en,1},
M. Casolino^{fx,ei}, C. Cassardo^{ek,el}, A. Castellina^{ek,em}, G. Castellini^{ed},
C. Catalano^{cd}, O. Catalano^{eh,en,1}, A. Cellino^{ek,em}, M. Chikawa^{fd},
G. Chiritoi^{ja}, M.J. Christl^{pg}, V. Connaughton^{pd}, L. Conti^{eo}, G. Continò^{ec,en},
G. Cordero^{ha}, G. Cotto^{ek,el}, H.J. Crawford^{pa}, R. Cremonini^{el}, S. Csorna^{ph},
S. Dagoret-Campagne^{ca}, C. De Donato^{ei}, C. de la Taille^{cb}, C. De Santis^{ei},
L. del Perai^{mc}, M. Di Martino^{em}, T. Djemil^{ac}, S.A. Djenas^{ah}, F. Dulucq^{cb},
M. Dupieux^{cd}, I. Dutan^{ja}, A. Ebersoldt^{db}, T. Ebisuzaki^{fx}, R. Engel^{db},
J. Eser^{pc}, K. Fang^{pb}, F. Fenu^{ek,el}, S. Fernández-González^{ma},
J. Fernández-Soriano^{mc}, S. Ferrarese^{ek,el}, D. Finco^{eo}, M. Flamini^{eo},
C. Fornaro^{eo}, R. Forza^{ek,el}, M. Fouka^{ab}, A. Franceschi^{ee}, S. Franchini^{md},
C. Fuglesang^{na}, J. Fujimoto^{fw}, M. Fukushima^{fg}, P. Galeotti^{ek,el},
E. García-Ortega^{ma}, G. Garipov^{kc}, E. Gascón^{ma}, J. Geary^{pd}, G. Gelmini^{pe},
J. Genci^{lb}, G. Giraudo^{ek}, M. Gonchar^{ka}, C. González Alvarado^{mb},
P. Gorodetzky^{cc}, N. Guardone^{ec,en}, F. Guarino^{ef,eg}, R. Guehaz^{aa},
A. Guzmán^{dd}, Y. Hachisu^{fx}, M. Haiduc^{ja}, B. Harlov^{kb}, A. Haungs^{db},
J. Hernández Carretero^{mc}, W. Hidber^{ha}, K. Higashide^{fr,fx}, D. Ikeda^{fg},
H. Ikeda^{fp}, N. Inoue^{fr}, S. Inoue^{fx}, A. Insolia^{ec,en}, F. Isgrò^{ef,ep}, Y. Itow^{fn},
T. Jammer^{dc}, E. Joven^{me}, E.G. Judd^{pa}, A. Jung^{cc}, J. Jochum^{dc}, F. Kajino^{fi},
T. Kajino^{fl}, S. Kalli^{af}, I. Kaneko^{fx}, D. Kang^{db}, F. Kanouni^{ag},
Y. Karadzhov^{ba}, J. Karczmarczyk^{ic}, M. Karus^{db}, K. Katahira^{fx},
K. Kawai^{fx}, Y. Kawasaki^{fx}, A. Kedadra^{aa}, H. Khaled^{aa}, B.A. Khrenov^{kc},
Jeong-Sook Kim^{ga}, Soon-Wook Kim^{ga}, Sug-Whan Kim^{gd}, M. Kleifges^{db},

P.A. Klimov^{kc}, D. Kolev^{ba}, I. Kreykenbohm^{da}, K. Kudela^{la}, Y. Kurihara^{fw},
 A. Kusenko^{fv,pe}, E. Kuznetsov^{pd}, M. Lacombe^{cd}, C. Lachaud^{cc},
 H. Lahmar^{aa}, F. Lakhdari^{ag}, O. Larsson^{fx,na}, J. Lee^{gc}, J. Licandro^{me},
 H. Lim^{gc}, L. López Campano^{ma}, M.C. Maccarone^{eh,en}, S. Mackovjak^{ob},
 M. Mahdi^{aa}, M. Manfrin^{ek,el}, D. Maravilla^{ha}, L. Marcelli^{ej}, J.L. Marcos^{ma},
 A. Marini^{ee}, K. Martens^{fv}, Y. Martín^{me}, O. Martínez^{hc}, G. Masciantonio^{ei},
 K. Mase^{fa}, R. Matev^{ba}, J.N. Matthews^{pi}, N. Mebarki^{ad},
 G. Medina-Tanco^{ha}, L. Mehrad^{ah}, M.A. Mendoza^{hd}, A. Merino^{ma},
 T. Mernik^{dd}, J. Meseguer^{md}, S. Messaoud^{aa}, O. Micu^{ja}, M. Mignone^{ek,el},
 J. Mimouni^{ad}, H. Miyamoto^{ek,el,1}, Y. Miyazaki^{fc}, Y. Mizumoto^{fl},
 G. Modestino^{ee}, A. Monaco^{ea,eb}, D. Monnier-Ragaigne^{ca}, J.A. Morales de
 los Ríos^{mc}, C. Moretto^{ca}, V.S. Morozenko^{kc}, B. Mot^{cd}, T. Murakami^{ff},
 B. Nadji^{aa}, M. Nagano^{fc}, M. Nagata^{fh}, S. Nagataki^{fx}, T. Nakamura^{fj},
 T. Napolitano^{ee}, D. Naumov^{ka}, R. Nava^{ha}, A. Neronov^{ob}, K. Nomoto^{fv},
 T. Nonaka^{fg}, T. Ogawa^{fx}, S. Ogiō^{fo}, H. Ohmori^{fx}, A.V. Olinto^{pb},
 P. Orleński^{id}, G. Osteria^{ef}, W. Painter^{db}, M.I. Panasyuk^{kc}, B. Panico^{ef},
 E. Parizot^{cc}, I.H. Park^{gc}, H.W. Park^{gc}, B. Pastircak^{la}, T. Patzak^{cc},
 T. Paul^{pf}, C. Pennypacker^{pa}, I. Pérez-Grande^{md}, F. Perfetto^{ef,eg}, T. Peter^{oc},
 P. Picozza^{ei,ej,fx}, T. Pierog^{db}, S. Pindado^{md}, L.W. Piotrowski^{pc},
 S. Piraino^{dd,eh}, L. Placidi^{eo}, Z. Plebaniak^{ic}, S. Pliego^{ha}, A. Pollini^{oa},
 E.M. Popescu^{ja}, P. Prat^{cc}, G. Prévôt^{cc}, H. Prieto^{mc}, M. Putis^{la},
 J. Rabanal^{ca}, A.A. Radu^{ja}, M. Rahmani^{ag}, P. Reardon^{pd}, M. Reyes^{me},
 M. Rezazadeh^{pb}, M. Ricci^{ee}, M.D. Rodríguez Frías^{mc}, F. Ronga^{ee},
 M. Roth^{db}, H. Rothkaehl^{id}, G. Roudil^{cd}, I. Rusinov^{ba}, M. Rybczyński^{ia},
 M.D. Sabau^{mb}, G. Sáez Cano^{mc}, H. Sagawa^{fg}, Z. Sahnoune^{ab}, A. Saito^{fj},
 N. Sakaki^{fo}, M. Sakata^{fi}, H. Salazar^{hc}, J.C. Sanchez^{ha}, J.L. Sánchez^{ma},
 A. Santangelo^{dd}, L. Santiago Cruz^{ha}, A. Sanz-Andrés^{md},
 M. Sanz Palomino^{mb}, O. Saprykin^{kb}, F. Sarazin^{pc}, H. Sato^{fi}, M. Sato^{fs},
 T. Schanz^{dd}, H. Schieler^{db}, V. Scotti^{ef,eg}, A. Segreto^{eh,en}, S. Selmane^{cc},
 D. Semikoz^{cc}, M. Serra^{me}, S. Sharakin^{kc}, T. Shibata^{fq}, H.M. Shimizu^{fm},
 K. Shinozaki^{dd}, T. Shirahama^{fr}, G. Siemieniec-Oziębło^{ib}, J. Sledd^{pg},
 K. Słomińska^{id}, A. Sobey^{pg}, I. Stan^{ja}, T. Sugiyama^{fm}, D. Supanitsky^{ha},
 M. Suzuki^{fp}, B. Szabelska^{ic}, J. Szabelski^{ic}, H. Tahia^{aa}, F. Tajima^{fe},
 N. Tajima^{fx}, T. Tajima^{fx}, Y. Takahashi^{fs}, H. Takami^{fw}, M. Takeda^{fg},
 Y. Takizawa^{fx}, M.C. Talai^{ac}, C. Tenzer^{dd}, O. Tibolla^{hf}, L. Tkachev^{ka},
 H. Tokuno^{ft}, T. Tomida^{fk}, N. Tone^{fx}, S. Toscano^{ob}, M. Traïche^{aa},
 R. Tsenov^{ba}, Y. Tsunesada^{fo}, K. Tsuno^{fx}, T. Tymieniecka^{ic}, Y. Uchihori^{fb},
 M. Unger^{db}, O. Vaduvescu^{me}, J.F. Valdés-Galicia^{ha}, P. Vallania^{ek,em},

G. Vankova^{ba}, C. Vigorito^{ek,el}, L. Villaseñor^{hb}, B. Vlcek^{mc}, P. von Ballmoos^{cd}, M. Vrabel^{lb}, S. Wada^{fx}, J. Watanabe^{fl}, S. Watanabe^{fs}, J. Watts Jr.^{pd}, M. Weber^{db}, R. Weigand Muñoz^{ma}, A. Weindl^{db}, T.J. Weiler^{ph}, T. Wibig^{ic}, L. Wiencke^{pc}, M. Wille^{da}, J. Wilms^{da}, Z. Włodarczyk^{ia}, T. Yamamoto^{fi}, Y. Yamamoto^{fi}, J. Yang^{gb}, H. Yano^{fp}, I.V. Yashin^{kc}, D. Yonetoku^{ff}, S. Yoshida^{fa}, R. Young^{pg}, I.S Zgura^{ja}, M.Yu. Zotov^{kc}, A. Zuccaro Marchi^{fx}

- ^{aa} Centre for Development of Advanced Technologies (CDTA), Algiers, Algeria
^{ab} Dep. Astronomy, Centre Res. Astronomy, Astrophysics and Geophysics (CRAAG), Algiers, Algeria
^{ac} LPR at Dept. of Physics, Faculty of Sciences, University Badji Mokhtar, Annaba, Algeria
^{ad} Lab. of Math. and Sub-Atomic Phys. (LPMPS), Univ. Constantine I, Constantine, Algeria
^{ae} Laboratory of Theoretical Physics LPT, University of Jijel, Jijel, Algeria
^{af} Department of Physics, Faculty of Sciences, University of M'sila, M'sila, Algeria
^{ag} Research Unit on Optics and Photonics, UROP-CDTA, Sétif, Algeria
^{ah} Telecom Lab., Faculty of Technology, University Abou Bekr Belkaid, Tlemcen, Algeria
^{ba} St. Kliment Ohridski University of Sofia, Bulgaria
^{ca} LAL, Univ Paris-Sud, CNRS/IN2P3, Orsay, France
^{cb} Omega, Ecole Polytechnique, CNRS/IN2P3, Palaiseau, France
^{cc} APC, Univ Paris Diderot, CNRS/IN2P3, CEA/Irfu, Obs de Paris, Sorbonne Paris Cité, France
^{cd} IRAP, Université de Toulouse, CNRS, Toulouse, France
^{da} ECAP, University of Erlangen-Nuremberg, Germany
^{db} Karlsruhe Institute of Technology (KIT), Germany
^{dc} Experimental Physics Institute, Kepler Center, University of Tübingen, Germany
^{dd} Institute for Astronomy and Astrophysics, Kepler Center, University of Tübingen, Germany
^{ea} Istituto Nazionale di Fisica Nucleare - Sezione di Bari, Italy
^{eb} Università degli Studi di Bari Aldo Moro and INFN - Sezione di Bari, Italy
^{ec} Dipartimento di Fisica e Astronomia - Università Catania, Italy
^{ed} Consiglio Nazionale delle Ricerche (CNR) - Istituto di Fisica Applicata Nello Carrara, Firenze, Italy
^{ee} Istituto Nazionale di Fisica Nucleare - Laboratori Nazionali di Frascati, Italy
^{ef} Istituto Nazionale di Fisica Nucleare - Sezione di Napoli, Italy
^{eg} Università di Napoli Federico II - Dipartimento di Scienze Fisiche, Italy
^{eh} INAF - Istituto di Astrofisica Spaziale e Fisica Cosmica di Palermo, Italy
^{ei} Istituto Nazionale di Fisica Nucleare - Sezione di Roma Tor Vergata, Italy
^{ej} Università di Roma Tor Vergata - Dipartimento di Fisica, Roma, Italy
^{ek} Istituto Nazionale di Fisica Nucleare - Sezione di Torino, Italy
^{el} Dipartimento di Fisica, Università di Torino, Italy
^{em} Osservatorio Astrofisico di Torino, Istituto Nazionale di Astrofisica, Italy

- ^{en} Istituto Nazionale di Fisica Nucleare - Sezione di Catania, Italy
^{eo} UTIU, Dipartimento di Ingegneria, Rome, Italy
^{ep} DIETI, Università degli Studi di Napoli Federico II, Napoli, Italy
^{fa} Chiba University, Chiba, Japan
^{fb} National Institute of Radiological Sciences, Chiba, Japan
^{fc} Fukui University of Technology, Fukui, Japan
^{fd} Kinki University, Higashi-Osaka, Japan
^{fe} Hiroshima University, Hiroshima, Japan
^{ff} Kanazawa University, Kanazawa, Japan
^{fg} Institute for Cosmic Ray Research, University of Tokyo, Kashiwa, Japan
^{fh} Kobe University, Kobe, Japan
^{fi} Konan University, Kobe, Japan
^{fj} Kyoto University, Kyoto, Japan
^{fk} Shinshu University, Nagano, Japan
^{fl} National Astronomical Observatory, Mitaka, Japan
^{fm} Nagoya University, Nagoya, Japan
^{fn} Institute for Space-Earth Environmental Research, Nagoya University, Nagoya, Japan
^{fo} Graduate School of Science, Osaka City University, Japan
^{fp} Institute of Space and Astronautical Science/JAXA, Sagamihara, Japan
^{fq} Aoyama Gakuin University, Sagamihara, Japan
^{fr} Saitama University, Saitama, Japan
^{fs} Hokkaido University, Sapporo, Japan
^{ft} Interactive Research Center of Science, Tokyo Institute of Technology, Tokyo, Japan
^{fu} Nihon University Chiyoda, Tokyo, Japan
^{fv} Kavli-IPMU (WPI), The University of Tokyo, Kashiwa, Japan
^{fw} High Energy Accelerator Research Organization (KEK), Tsukuba, Japan
^{fx} RIKEN, Wako, Japan
^{ga} Korea Astronomy and Space Science Institute (KASI), Daejeon, Republic of Korea
^{gb} Ewha Womans University, Seoul, Republic of Korea
^{gc} Sungkyunkwan University, Seoul, Republic of Korea
^{gd} Center for Galaxy Evolution Research, Yonsei University, Seoul, Republic of Korea
^{ha} Universidad Nacional Autónoma de México (UNAM), Mexico
^{hb} Universidad Michoacana de San Nicolas de Hidalgo (UMSNH), Morelia, Mexico
^{hc} Benemérita Universidad Autónoma de Puebla (BUAP), Mexico
^{hd} Centro de Desarrollo Aeroespacial - Instituto Politécnico Nacional (CDA-IPN), Mexico
^{he} Universidad Autónoma de Chiapas (UNACH), Chiapas, Mexico
^{hf} Centro Mesoamericano de Física Teórica (MCTP), Mexico
^{ia} Jan Kochanowski University, Institute of Physics, Kielce, Poland
^{ib} Jagiellonian University, Astronomical Observatory, Krakow, Poland
^{ic} National Centre for Nuclear Research, Lodz, Poland
^{id} Space Research Centre of the Polish Academy of Sciences (CBK), Warsaw, Poland
^{ja} Institute of Space Science ISS, Magurele, Romania
^{ka} Joint Institute for Nuclear Research, Dubna, Russia
^{kb} Central Research Institute of Machine Building, TsNIIMash, Korolev, Russia

- ^{kc} Skobeltsyn Institute of Nuclear Physics, Lomonosov Moscow State University, Russia
- ^{la} Institute of Experimental Physics, Kosice, Slovakia
- ^{lb} Technical University Kosice (TUKE), Kosice, Slovakia
- ^{ma} Universidad de León (ULE), León, Spain
- ^{mb} Instituto Nacional de Técnica Aeroespacial (INTA), Madrid, Spain
- ^{mc} Universidad de Alcalá (UAH), Madrid, Spain
- ^{md} Universidad Politécnica de madrid (UPM), Madrid, Spain
- ^{me} Instituto de Astrofísica de Canarias (IAC), Tenerife, Spain
- ^{na} KTH Royal Institute of Technology, Stockholm, Sweden
- ^{oa} Swiss Center for Electronics and Microtechnology (CSEM), Neuchâtel, Switzerland
- ^{ob} ISDC Data Centre for Astrophysics, Versoix, Switzerland
- ^{oc} Institute for Atmospheric and Climate Science, ETH Zürich, Switzerland
- ^{pa} Space Science Laboratory, University of California, Berkeley, USA
- ^{pb} University of Chicago, USA
- ^{pc} Colorado School of Mines, Golden, USA
- ^{pd} University of Alabama in Huntsville, Huntsville, USA
- ^{pe} University of California (UCLA), Los Angeles, USA
- ^{pf} Lehman College, City University of New York (CUNY), USA
- ^{pg} NASA - Marshall Space Flight Center, USA
- ^{ph} Vanderbilt University, Nashville, USA
- ^{pi} University of Utah, Salt Lake City, USA

¹ Corresponding authors: Mario Bertaina (E-mail address: bertaina@to.infn.it), Rossella Caruso (E-mail address: rossella.caruso@ct.infn.it), Osvaldo Catalano (E-mail address: catalano@ifc.inaf.it), Hiroko Miyamoto (E-mail address: miyamoto@to.infn.it)

Abstract

JEM-EUSO is a space mission designed to investigate Ultra-High Energy Cosmic Rays and Neutrinos ($E > 5 \cdot 10^{19}$ eV) from the International Space Station (ISS). Looking down from above its wide angle telescope is able to observe their air showers and collect such data from a very wide area. Highly specific trigger algorithms are needed to drastically reduce the data load in the presence of both atmospheric and human activity related background light, yet retain the rare cosmic ray events recorded in the telescope. We report the performance in offline testing of the first level trigger algorithm on data from JEM-EUSO prototypes and laboratory measurements observing different light sources: data taken during a high altitude balloon flight over Canada, laser pulses observed from the ground traversing the real atmosphere, and model landscapes reproducing realistic aspect ratios and light

conditions as would be seen from the ISS itself. The first level trigger logic successfully kept the trigger rate within the permissible bounds when challenged with artificially produced as well as naturally encountered night sky background fluctuations and while retaining events with general air-shower characteristics.

Key words: JEM-EUSO, trigger system, FPGA, nightglow background

1. Introduction

Ultra-High Energy Cosmic Rays (UHECR) are observed as Extensive Air Showers (EAS) in the atmosphere surrounding Earth. They are rare events, and the higher their energy, the rarer they get. The greatest mystery surrounding them is their origin, but also their nature remains contentious. High statistics and high quality data are needed to make progress on both fronts, which means scanning the largest possible volume of atmosphere for EAS. The current ground based experiments run up against natural boundaries limiting their expansion and present difficulties when comparing data obtained in northern and southern latitudes, as the fraction of common sky is limited. Therefore, space based instruments observing the atmosphere from above with full-sky coverage have long been considered the logical next step in the evolution of UHECR experiments [1].

The International Space Station (ISS) with its existing infrastructure and support systems is a natural first step on this way into space, and JEM-EUSO [2] is a scientific mission under development with the aim of identifying the astrophysical origin and nature of UHECRs from the ISS. JEM-EUSO detects UHECR induced EAS by looking down onto the earth atmosphere. It has a telescope with a large ($\pm 30^\circ$) Field of View (FoV) imaging the atmosphere below the ISS onto an array of UV sensitive Multi-Anode Photomultiplier Tubes (MAPMTs) [3]. The MAPMTs (Hamamatsu Photonics R11265-03-M64) have 8×8 pixels and for readout purposes 2×2 MAPMTs are grouped into one Elementary Cell (EC). The First Level Trigger (FLT), which is the subject of this article, works at the level of these ECs. Nine ECs form one Photo-Detector Module (PDM), which is the basic unit for the Second Level Trigger (SLT). The Focal Surface (FS) is organised in 137 PDMs. Together these PDMs cover the FS of the telescope with $\sim 3.2 \cdot 10^5$ MAPMT pixels. A detailed description of the electronics and data acquisition for JEM-EUSO can be found in [4], while a sketch of the structure of the FS is shown in

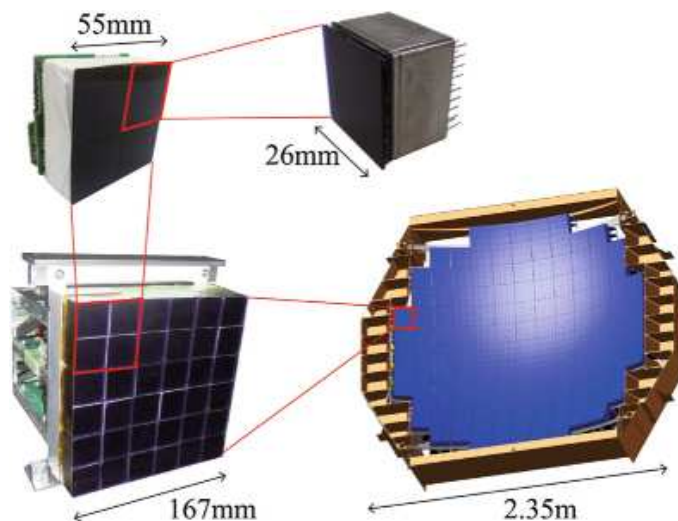


Figure 1: Structure of the Focal Surface. The 2.5 m surface is divided in 137 PDM modules. Each PDM is filled with 9 ECs, with 4 MAPMTs each. The bottom left corner shows the prototype of the mechanical structure with 36 MSPMTs installed. Figure taken from [4].

30 Fig. 1.

31 The observational concept of JEM-EUSO [5] is based on recording both
 32 the fluorescence light emitted during the evolution of EAS as well as the
 33 reflected Čerenkov light if the EAS' Čerenkov cone hits a reflective surface
 34 as it reaches the ground. EAS from the interaction of UHECRs or neutrinos
 35 in the atmosphere will - for 10^{20} eV EAS - typically result in a few thou-
 36 sand photons detected by the JEM-EUSO detector within a few hundred
 37 microseconds. Owing to the large FoV the expected rate of such ultra high
 38 energy EAS are approximately one per day. Depending on both the energy
 39 and the zenith angle of the EAS, images may be contained inside a single
 40 EC or may cross a few PDMs as they are imaged onto across the FS. EAS
 41 develop within the lowest 15 km of the Earth atmosphere, so that their dis-
 42 tance to the ISS, which orbits earth at a height above ground of about 400
 43 km, can be considered unchanging whatever an individual EAS' zenith angle
 44 happens to be. With that EAS' angular speed across the FS to first order
 45 only depends on the EAS' propagation direction relative to the respective FS
 46 pixels' direction of view. As EAS traverse the atmosphere at essentially the
 47 speed of light, and from the height of the ISS a single square MAPMT pixel's
 48 FoV's diagonal measures roughly 750 m on the ground, it takes about $2.5 \mu s$

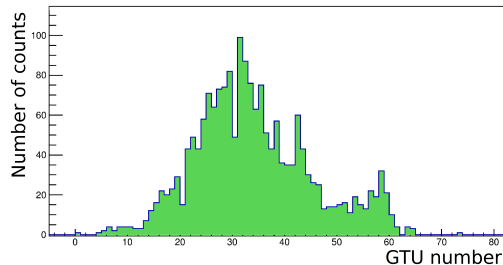


Figure 2: Light curve (number of photoelectron counts) integrated over the shower profile and plotted over time along the shower axis for a simulated UHECR EAS of 2×10^{20} eV (no background is added). Time is measured in GTUs (see Section 2).

49 for horizontal EAS' image to traverse the diagonal of a MAPMT pixel. As
 50 bandwidth for data transmission from the ISS back to Earth is limited, 2.5
 51 μ s, the so-called Gate Time Unit (GTU), was adopted as the basic unit for
 52 digitization at JEM-EUSO. Given the distance between EAS and ISS, JEM-
 53 EUSO must be able to detect single photons. The front-end electronics works
 54 in single photon-counting mode, which means that HV and electronics gain
 55 are adjusted such that after digitization one digital increment corresponds to
 56 one photoelectron (PE) count released from the MAPMT's photocathode.

57 In this paper we discuss the FLT algorithm specific to the identification
 58 of UHECR and neutrino induced EAS. Fig. 2 shows the temporal evolution
 59 in units of GTU of the MAPMT signal for typical simulated proton EAS of
 60 energy $2 \cdot 10^{20}$ eV, viewed by the JEM-EUSO telescope under an angle of
 61 60° . [EAS simulations are performed using the ESAF \[6\] package adapted](#)
 62 [to the JEM-EUSO instrument](#). In Fig. 3, the top panel shows the spacial
 63 distribution of simulated EAS scintillation light emission projected back onto
 64 the Earth's surface for EAS with a common energy of $E = 10^{20}$ eV traversing
 65 the atmosphere under zenith angles of (a) $\theta = 30^\circ$, (b) $\theta = 60^\circ$ and (c)
 66 $\theta = 75^\circ$. The inset in the lower left corner of this panel puts these showers
 67 into the context of the FoV of the whole FS of JEM-EUSO. The bottom panel
 68 presents the image of the EAS in (b) as it would be seen by the JEM-EUSO
 69 telescope: the optics inverts the direction of motion, and the photon counts
 70 per pixel are integrated over the EAS duration [which is of the order of 100](#)
 71 [\$\mu\$ s](#).

72 Looking down from the ISS the FLT has to identify these events in the
 73 presence of various backgrounds: UV albedo, transient atmospheric phenom-
 74 ena, and artificial light sources in cities, along transportation networks, and

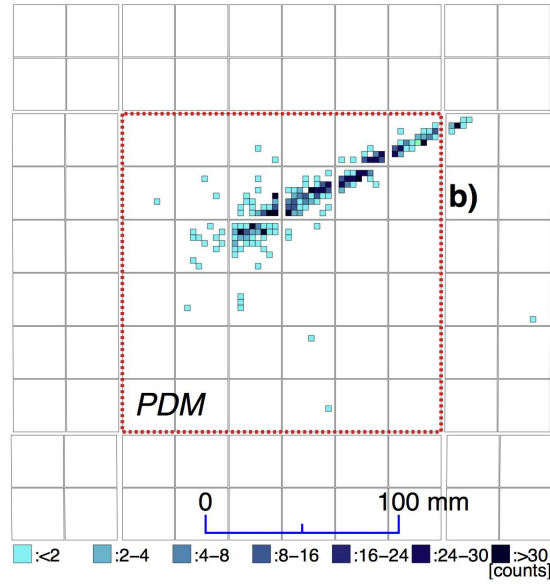
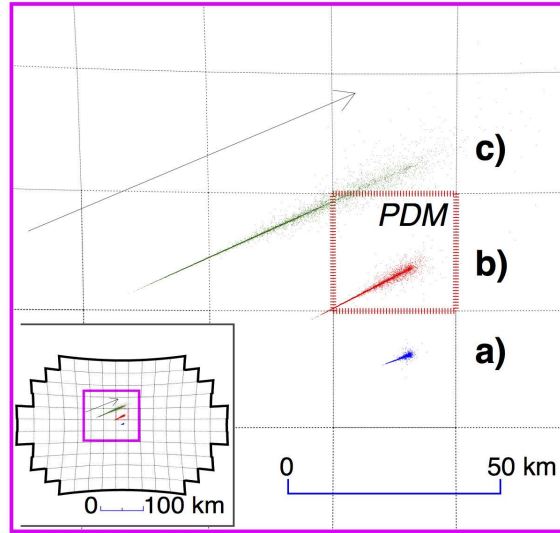


Figure 3: The top panel shows the 3 EAS with the same energy of $E = 10^{20}$ eV but impinging on the atmosphere under different zenith angles of (a) $\theta = 30^\circ$, (b) $\theta = 60^\circ$ and (c) $\theta = 75^\circ$. The most inclined EAS last $\sim 250 \mu s$. The arrow indicates the direction of the EAS transit on the FS. The inset on the bottom left and the grey grid shows how the FoV is imaged on the telescope's FS. The distance scale on this panel refers to the distance the shower develops over as projected onto the Earth surface. The bottom panel shows the image (inverted by the optics) on shower (b) as recorded (integrated over time) by the JEM-EUSO telescope. The distance scale here refers to distance on the FS. The regions enclosed by thick dashed lines in both panels refer to the same PDM. Image taken from [7]. UV background is not added in these plots.

75 on ships and airplanes. The ISS is moving at about 7.6 km/s so that sta-
76 tionary light sources on the ground stay within the FoV of a single pixel for
77 about 70 ms. Such anthropogenic lights, as for example cities, are in the FoV
78 on average during only $\sim 10\%$ of an ISS orbit [7]. Transient Luminous Events
79 (TLEs) within the atmosphere, like electric discharges (Elves, Sprites, Blue
80 Jets and lightning) as well as meteors will have their own triggering schemes
81 to support a separate science program with JEM-EUSO and will be sup-
82 pressed by the UHECR and neutrino oriented FLT on the basis of time and
83 light intensity structures. The expected rate of TLEs is $\sim 700/\text{day}$ [8]. The
84 greatest uncertainty is associated with the very slowly varying backgrounds
85 associated with the albedo of the atmosphere: its scattering and reflection
86 of starlight - light reflected from the moon and planets - and airglow. On a
87 clear night the resulting diffuse flux of such photons is expected to amount to
88 between 300 and 1000 photons $\text{m}^{-2} \text{ns}^{-1} \text{sr}^{-1}$, an expectation derived from
89 existing measurements [9, 10].

90 In this paper we show the results of the offline testing of the current
91 JEM-EUSO FLT concept using data from three main sources rather than
92 simulation: data collected during a high altitude balloon flight over Canada
93 (EUSO-Balloon), laser shots recorded in coincidence with a ground based
94 JEM-EUSO prototype (EUSO-TA), and data taken in a laboratory setup
95 where realistic background scenarios can be explored (EUSO@TurLab).

96 2. Technical requirements

97 As mentioned before, working on the ISS imposes severe bandwidth con-
98 straints on data transfer to the ground. On top of that there is a ~ 1 kW
99 limit on power consumption for the whole telescope, including the readout
100 and trigger electronics, high voltage for the MAPMTs, and monitoring. This
101 constraint for example means that triggering cannot be substituted for by
102 massive only computing. Data rate considerations also played into choosing
103 a GTU of $2.5 \mu\text{s}$ for digitization in time [and the number of 128 GTUs per](#)
104 [packet](#), meaning that each event record will contain the timing evolution of
105 a signal over a time span of $320 \mu\text{s}$.

106 Since the ISS is far above the parts of the atmosphere where EAS develop,
107 the MAPMTs have to be able to detect faint signals using photon-counting.
108 Therefore, 8 bit full scale per pixel is sufficiently large. Under these conditions
109 the total data rate from the telescope before the FLT would be of order
110 $3.2 \cdot 10^5 \text{ pixel/FS} \times 4 \cdot 10^5 \text{ GTU/s} \times 8 \text{ bit/pixel} \approx 1 \text{ Tbps}$. To achieve the

111 required overall data reduction of $\sim 3 \cdot 10^6$ the FLT will have to reduce the
112 trigger rate to ~ 1 Hz/EC, and the PDM based second level trigger to ~ 0.1
113 Hz/FS [11, 12].

114 In the following section, specifics of the FLT logic aimed at detecting
115 UHECR and neutrino induced EAS, which are the main scientific objective
116 of the JEM-EUSO mission, are considered. While TLEs and other bright but
117 slow atmospheric events are part of the exploratory objectives of the mission,
118 we will not consider them here.

119 **3. The 1st Trigger Level: Persistency Tracking Trigger**

120 Persistency is a measure of how long in time a signal “persists” or stays
121 within the FoV of a particular MAPMT pixel. As detailed above a GTU
122 roughly reflects the time horizontal EAS right under the ISS need to travel
123 the diagonal of a MAPMT pixel. To cross the FoV of an EC, where the FLT
124 operates, takes up to $45 \mu\text{s}$ for EAS, milliseconds for lightning, hundreds of
125 milliseconds for meteors, and seconds for cities or airplanes. These differences
126 in persistency and the fact that the signal moves from pixel to pixel as EAS
127 pass through the FoV of the telescope were exploited in designing the FLT
128 logic, which is described in [13]. Here we give a summary of how an EAS
129 trigger is formed at the EC/FLT level.

130 Unless EAS develop along the line of sight of the telescope, the image
131 of their fluorescence trails in the atmosphere can be tracked across the FS.
132 Tracking discriminates EAS images against accidental coincidences of back-
133 ground light fluctuations.

134 To decide if a single MAPMT pixel is seeing signal above a slowly vary-
135 ing, non-negligible background, this background level has to be estimated.
136 Two different approaches were pursued: The pixel-based estimate sets one
137 threshold for a whole MAPMT. To obtain this threshold the average over
138 a 128 GTU data packet is calculated for each pixel in the MAPMT, and
139 the maximum of these 64 averages becomes the background estimate and
140 threshold for triggering in the next 128 GTU packet. Stationary or slowly
141 moving anthropogenic light sources within the atmosphere are automatically
142 suppressed by this method. The group-based estimate divides the whole EC
143 into 32 groups of 2×4 pixels, calculates the 128 GTU averages per group,
144 and chooses the maximum of those 32 averages as the threshold for all pixels
145 in the EC during the next 128 GTU packet. The threshold here is a digital
146 value as all calculations are done after digitization. No analog thresholds

147 are used. The results presented in this paper are based on the pixel-based
148 estimate which turned out to be better performing overall.

149 For tracking purposes each MAPMT's pixels are grouped into square 3×3
150 cells. Each pixel belongs to more than one cell, but since cells do not span
151 MAPMT borders, pixels along the edges and in particular at the corners of
152 each MAPMT belong to fewer cells than the central pixels. The first panel
153 in Fig. 4 shows three such overlapping cells on a single MAPMT's pixel grid
154 outlined in dark orange. Since it includes neighboring MAPMTs' pixels, the
155 3×3 pixel patch surrounded by the dashed grey line on the other hand does
156 not constitute a cell. A total of 36 cells exists within each MAPMT. Each
157 pixel for which its digitized signal in a certain GTU of a 128 GTU packet
158 surpasses the threshold value $n_{\text{thr}}^{\text{pix}}$ for that MAPMT (determined from the
159 data in the preceding 128 GTU) contributes to each of the cells it participates
160 in. Apart from the pixel level signal threshold there also is a cell level signal
161 threshold $n_{\text{thr}}^{\text{cell}}$. For a typical background level of one PE per GTU per pixel
162 these thresholds $n_{\text{thr}}^{\text{pix}}$ and $n_{\text{thr}}^{\text{cell}}$ would normally be set to 3 and 31, respectively.

163 Persistency at the pixel level is evaluated based on two more paramete-
164 rters that unlike those introduced above do not depend on the background
165 situation: a pre-determined range of consecutive GTUs N_{pst} over which per-
166 sistency is to be evaluated, and a limit N_{ctd} on the number of GTUs within
167 that range for which pixels in the cell are above threshold. Standard values
168 for the pixel related parameters N_{pst} and N_{ctd} are 5 and 3 GTUs, respec-
169 tively. These values were determined by means of simulations of EAS signals
170 and of preliminary tests on MAPMT fluctuations with the aim of keeping
171 EAS signals and rejecting background fluctuations. Persistency of a signal
172 at the EC level is also monitored and similarly checked by two parameters
173 for a maximum allowed number of GTUs above threshold $N_{\text{GTU}}^{\text{thr}}$ in a GTU
174 range N_{GTU} . Too many GTUs with signal indicate high persistency, which
175 is the hallmark of non-EAS induced events like lightning or meteors. This
176 GTU range is started at the GTU in which for the first time a cell threshold
177 is surpassed. Typical values for EAS identification are $N_{\text{GTU}} = 73$ and $N_{\text{GTU}}^{\text{thr}}$
178 $= 72$. These two values were decided according to the following considera-
179 tions. N_{GTU} is determined by the number of GTUs remaining after the first
180 trigger till the end of the packet. For technical reasons it was decided to have
181 the trigger at GTU 55 of a packet. The $N_{\text{GTU}}^{\text{thr}}$ indicates that all the events
182 are accepted unless the PDM continues triggering every GTU after the first
183 trigger till the end of the packet. Both values will be fine tuned in future, if
184 needed. In particular $N_{\text{GTU}}^{\text{thr}}$ can be easily shortened by a few GTUs without

185 [impacting the trigger efficiency on EAS.](#)

186 As mentioned above power consumption is a major constraint on the ISS.
187 The current implementation of the FLT was programmed into and tested
188 on a Xilinx Virtex6 model XC6VLX240T [14] FPGA. Given that it required
189 only $\sim 7\%$ of this FPGA's resources to accommodate the logic needed for 1
190 EC, it is expected that one such FPGA can host all 9 ECs belonging to one
191 PDM. The graphic in the following figure reflects the FPGA architecture in
192 its reference to the FPGA's various adders.

193 Fig. 4 uses an event recorded by EUSO@TurLab ² to illustrate how a
194 FLT is formed. The background estimate was derived from the the preceding
195 GTU packet as $n_{\text{thr}}^{\text{pix}} = 5$ and $n_{\text{thr}}^{\text{cell}} = 65$; the average background light level
196 for that packet was of order 3.4 PE/GTU/pixel. Using the standard values
197 of $N_{\text{ctd}} = 3$ and $N_{\text{pst}} = 5$, the graphic follows the cell's pixels' recorded PE
198 counts for an EAS-like event created by a line of LEDs mimicking an almost
199 vertical shower mostly staying in the FoV of the cell's central pixel. In the
200 first panel of Fig. 4 the cell is highlighted in dark orange on the MAPMT's
201 pixel map. The next five sub-panels of the figure after the MAPMT pixel
202 overview show two pixel maps each for that same cell. The five sub-panels
203 represent the five successive GTUs following the cell's first threshold crossing.
204 The pixel map on the left in each sub-panel shows the raw PE counts recorded
205 per MAPMT pixel in the respective GTU. Using the estimated $n_{\text{thr}}^{\text{pix}} = 5$
206 PE background as threshold then leads to the pattern of threshold-crossing
207 pixels displayed on the right of the sub-panel with each pixel's background
208 subtracted PE signal estimates. The sum of that signal above background
209 is then compared to the cell threshold $n_{\text{thr}}^{\text{cell}} = 65$ PE. In summary: for the
210 chosen cell and its five GTUs after the cell's threshold crossing, at least one
211 pixel in the cell crosses the pixel threshold for each GTU, and the total signal
212 strength accumulated within this cell in each GTU is enough to contribute
213 to the EC wide evaluation of the event. Therefore, at GTU step 5 the
214 corresponding adder (T) is incremented. The EC-wide check with regard to
215 the GTUs during which the signal passes through all the other EC cells is
216 summarized in the last panel, where the content of the adder T is finally
217 checked before a FLT is issued (or not) to the PDM for second level trigger
218 purposes.

219 Persistence is the main concept behind the FLT implementation. In the

²see Section 4.1 and Fig. 11 for more details.

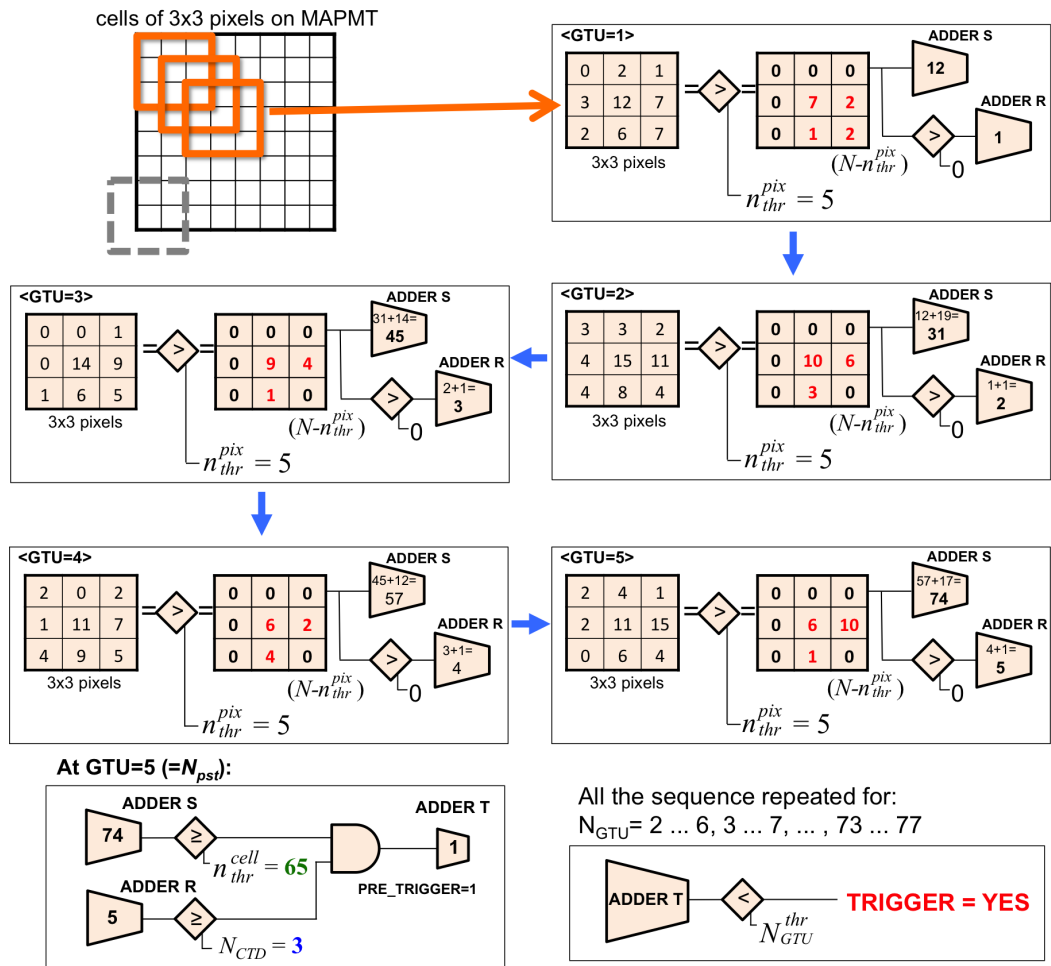


Figure 4: The FLT implementation at the level of the 3x3 cells. See text for details.

220 following section we will discuss how this current implementation performs
221 in the presence of background, using data recorded with EC modules in dedi-
222 cated experiments reflecting different aspects of space based EAS observation
223 in the Earth atmosphere.

224 **4. FLT Tests using experimental data**

225 The trigger efficiency as a function of EAS energy (commonly referred
226 to as the trigger efficiency curve) captures an important aspect of the ex-
227 periment’s sensitivity. Several publications already discussed the expected
228 JEM-EUSO sensitivity given the current FLT implementation, but so far
229 they were purely based on MC simulations [5, 7, 15]. These simulations all
230 assumed Poisson fluctuations on a UV background intensity that is constant
231 and uniform across the FS.

232 In this section we report on tests performed offline using data taken with
233 actual ECs in three very different environments, each addressing specific chal-
234 lenges JEM-EUSO is expected to face during observation from the ISS: data
235 collected by the EUSO-Balloon flight in 2014 [16], measurements performed
236 by EUSO@TurLab at TurLab [17], and observations in coincidence with a
237 Telescope Array (TA) air fluorescence detector by EUSO-TA [18]. These
238 data sets allow to test the trigger system in very different and complemen-
239 tary ways. EUSO@TurLab provides the possibility to control lighting and
240 create realistic event patterns and persistencies, EUSO-Balloon takes data
241 under space-like conditions, and EUSO-TA allows comparison with a well
242 calibrated existing ground-based fluorescence detector.

243 *4.1. Tests with TurLab measurements*

244 The two main aspects of the FLT that were tested at TurLab, [located at](#)
245 [the Physics Department of the University of Turin \(Italy\)](#), were the adequacy
246 of its background estimation and the ability to trigger on EAS while sup-
247 pressing other signatures, [such as cities, meteors, lightnings, discontinuities](#)
248 [in the luminosity due to the presence of clouds, variation in soil condition,](#)
249 [moon phase, etc.](#) All these phenomena have variable intensity, duration and
250 extension. Table 1 gives typical values expected for JEM-EUSO for a subset
251 of these conditions which have been reproduced at TurLab to test the trigger
252 logic.

253 Being 15m under ground, the ambient light level in the TurLab laboratory
254 [17] is several orders of magnitude lower than that of the darkest night sky.

light source	intensity (cts/pix/GTU)	duration	extension	variability
UV glow	0.5 - 5	orbit	EC	water, soil, cloud
Urban	3 - 30	seconds	pixel - EC	village - city
EAS	3 - 30	$\sim 100\mu\text{s}$	PMT (track)	EAS energy
Meteor	3 - 100	seconds	EC (track)	magnitude

Table 1: Variability of the signal expected for JEM-EUSO due to different light sources in the FoV of the telescope, ranging from steady UV nightglow to localized and impulsive light bursts such as cities, EAS, meteors. The maximum luminosity of meteors is here defined by the saturation of the front-end electronics.

255 Using artificial light sources therefore puts the ambient light levels as well as
 256 the distribution of light in the lab under the control of researchers.

257 At TurLab a rotating tank of 5 m diameter provides the stage on which
 258 light emitting as well as light reflecting installations are made. EUSO@TurLab
 259 consists of one EC hung off-center from the ceiling above this rotating tank.
 260 While in principle the EC can be moved radially it was kept at a radius of
 261 roughly 2 m from the center of the tank. The optics imaged 1 cm^2 on the
 262 tank's surface onto one pixel 2 m above the tank surface, giving it a FoV
 263 of the order of 10^{-5} sr, which is only one order of magnitude larger than a JEM-
 264 EUSO's pixel. This means that if the adjustable speed of the tank rotation
 265 were to be around two minutes, the time it takes a stationary source on the
 266 tank surface to cross a pixel would be the same as it will be for JEM-EUSO
 267 looking down on Earth from the ISS.

268 As outlined before, the data acquisition (DAQ) in JEM-EUSO will be a
 269 seamless sequence of 128 GTU long packets. At EUSO@TurLab the EC's
 270 ASIC is read out by a test board which transfers the data to a PC, and
 271 this system both limits a data packet to 100 GTUs and imposes a ~ 50 ms
 272 deadtime between two consecutive packet acquisitions. In other words, at
 273 EUSO@TurLab $100\text{ GTUs} = 250\ \mu\text{s}$ of data are taken every ~ 50 ms, and a
 274 stationary light source on the tank surface would have moved through 50%
 275 of the FoV of a pixel during that deadtime if the tank rotated with a period
 276 of 2 min. It was not possible to synchronize the DAQ with the tank rotation,
 277 because it was not foreseen by the control system of the tank. Naturally, the
 278 synchronization would have allowed to determine exactly the location in the
 279 tank responsible for each trigger.

280 Fig. 5 shows the various components of the TurLab setup. It shows the

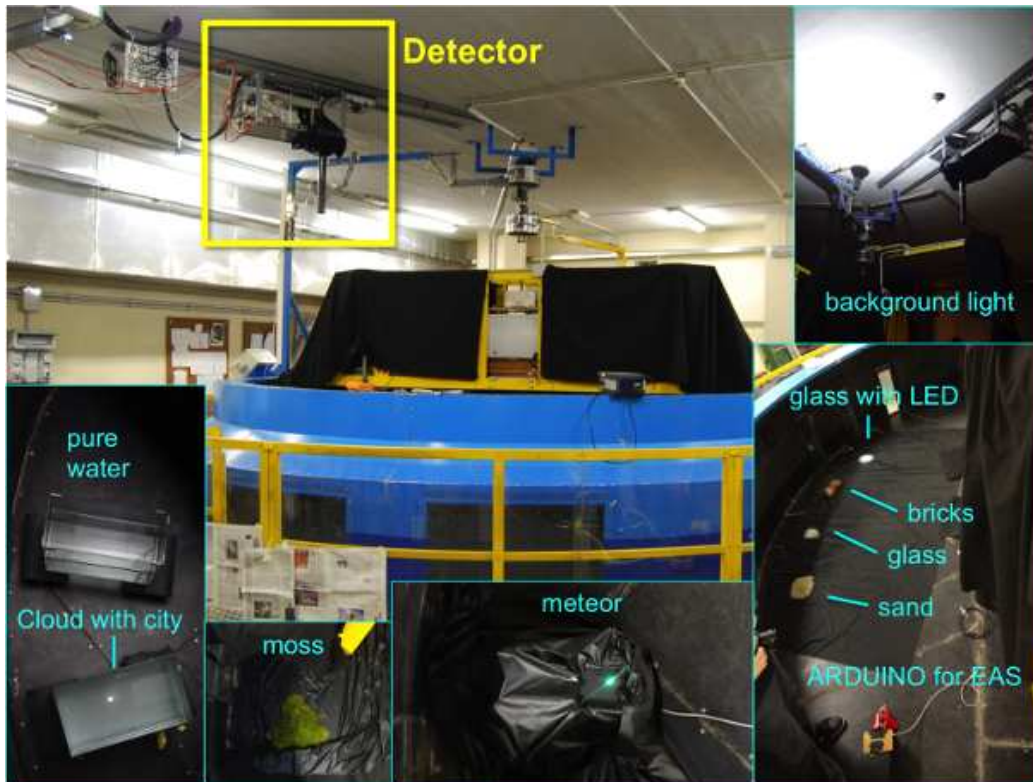


Figure 5: The TurLab rotating tank. The black tube on the ceiling shows the collimator of the experimental setup used to mimic the JEM-EUSO telescope. Light sources and materials used to mimic other phenomena are shown as well.

281 EC suspended from the ceiling, and various installations on the tank surface
282 designed to emit or reflect light in ways that mimic both anthropogenic and
283 natural lighting situations as they would be seen by JEM-EUSO from the
284 ISS (see Table 1). Light scattered or reflected from the atmosphere back into
285 space - the Earth's *albedo* - depends on atmospheric conditions like e.g. the
286 presence or absence of clouds, the reflectivity of the Earth's local surface, and
287 lighting conditions like the phase of the moon³ or the presence and density
288 of human habitation.

289 In Fig. 5 one can also see how sand, moss, ground glass, pure water,
290 and a brick were used to mimic the reflection of night-sky light from soils,
291 forests, snow, water, and rocky surfaces, respectively. Water clouded by dis-
292 solved particles and illuminated from below is used to mimic clouds, and if
293 illuminated from below cloud cover over e.g. a city. An oscilloscope screen
294 displaying Lissajous traces mimics meteor tracks. As lighting can be con-
295 trolled, the TurLab tank allows to verify the performance of the background
296 estimation under realistically varying lighting conditions. Fig. 6 and Fig. 7
297 show two examples of recordings of such features with EUSO@TurLab.

298 In Fig. 6 LED light reflected from ground glass is used to simulate the
299 distributed individual light sources of a city. Each of the four frames in each
300 sub-panel refers to one of the four MAPMTs in the EC. The upper panels
301 show the respective MAPMT's integrated PE counts, in other words the
302 light curve of a city passing through the FoV of the EC. The city entering
303 and exiting the MAPMT's FoV as time progresses is clearly visible in each
304 MAPMT's light curve. The lower row shows 2D pixel maps for the EC's
305 MAPMTs, with the PE counts per pixel for just one GTU on the left, 10
306 GTUs in the center, and 100 GTUs on the right. The red lines in the light
307 curves show the range of GTUs that are used, with the single GTU pixel maps
308 being the first GTU under both red lines; the start times of this integration
309 is the same for all three ranges. Fig. 7 shows the data recorded while passing
310 over the oscilloscope repeating a straight line Lissajous figure taking about
311 one second to complete. While the complete picture emerges after integrating
312 over 1500 GTUs (right panel), the signal still is contained in a single pixel
313 when integrating over only 10 GTUs (center panel).

314 An Arduino board [19] controlling a line of 10 white LEDs was used to
315 mimic a single EAS propagating through the atmosphere at the speed of

³Fluorescence observation of EAS is not possible during daytime.

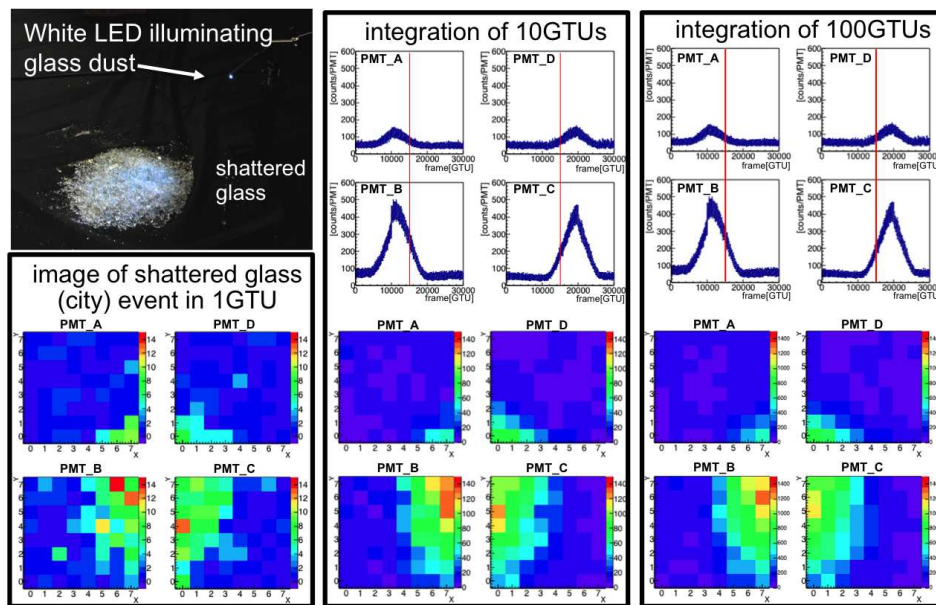


Figure 6: Reproduction of an extended light source, like in case of a city. Top-left plot is a picture of the shattered glass; bottom left plot is the image detected by the MAPMTs in 1 GTU. The right-top plots shows the temporal evolution of the same scene with different time integrations (10 and 100 GTUs). The bottom plot shows one frame per integration taken at the time indicated by the red line in the above plots.

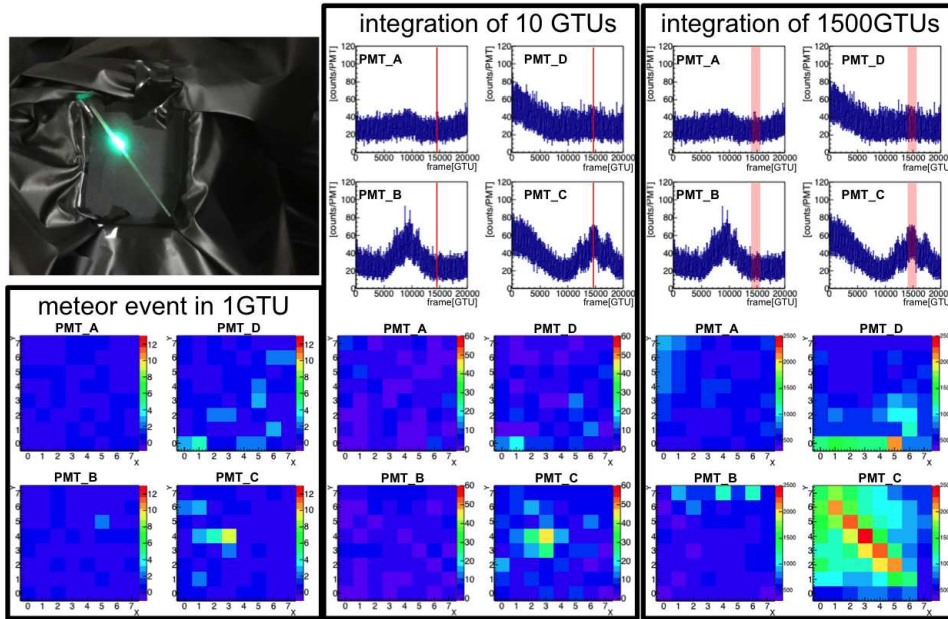


Figure 7: Reproduction of a meteor-like track. See Fig. 6 for details about the meaning of each plot in the figure.

316 light, resulting in a total duration of about 40 GTUs. As can be seen in
 317 Fig. 8 this signal does no longer stay within one pixel during 10 GTUs, with
 318 the center of light moving visibly between subsequent GTUs.

319 The FLT estimates the background for the current data packet from the
 320 data collected in the preceding data packet. To mitigate possible adverse
 321 effects of the DAQ-imposed deadtime between the acquisition of consecutive
 322 packets on background estimation the tank rotation was slowed to complete
 323 one rotation in 9 min, reducing the offset of a stationary light source between
 324 consecutive acquisition packets from 50% of a pixel to roughly 10% of a pixel;
 325 with the JEM-EUSO DAQ a 128 GTU offset at ISS speed would correspond
 326 to 0.5% of the pixel size projected onto the ground. Given the deadtime
 327 between the 100 GTU acquisition packets a total of ~ 3 seconds of data is
 328 collected during one 9 minute rotation.

329 The DAQ at TurLab collects that data “as is”: it simply reads out the
 330 PE counts for each MAPMT pixel in each GTU from the EC’s ASIC and
 331 writes them to disk. The subsequent trigger simulation is then implemented

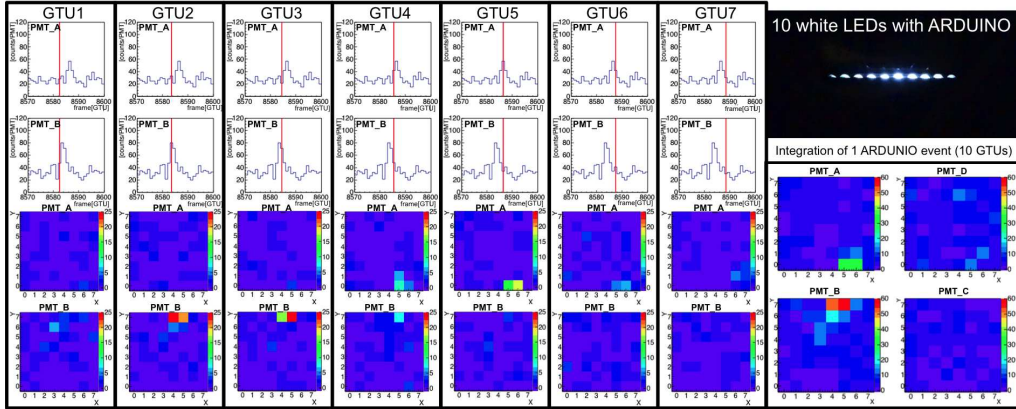


Figure 8: Reproduction of a cosmic ray-like track. Top-right picture shows the integrated light sequence reproducing a cosmic-ray track. Bottom-right plot shows the integrated number of counts during the light sequence. The left part of the figure displays 7 frames of 1 GTU each taken during the reproduction of the track. The time at which the frames are taken is shown in the above corresponding plots which present the time evolution of the total number of counts recorded by the MAPMT.

332 in VHDL⁴ according to the schema described in [13].

333 The light collected on one of the EC’s MAPMTs during a complete 9
 334 minute rotation of the tank is shown in the upper panel of Fig. 9. Changes
 335 in the background light level are clearly seen, and the various contraptions
 336 that precipitate them are labeled in the figure. The two bridges refer to the
 337 footbridges to cross the tank which, despite being covered by some black
 338 fabric, are a source of quite variable light reflection. In general the black
 339 fabric was used to make as dark as possible specific regions of the tank to
 340 help increase the dynamic range of the light intensity seen by the MAPMTs
 341 during the tank rotation. Pure water in a little transparent tank was used
 342 to mimic a mirror-like condition which induces much higher reflection. The
 343 yellow bar is a pole on the rotating tank which passes a few cm below the
 344 collimator, thus filling a significant portion of the FoV of the detector for a
 345 short time. The second panel of Fig. 9 shows the average PE count in the
 346 preceding 100 GTU packet for the pixel with the maximal average count in
 347 that same MAPMT, which is the value used for the threhsold setting in the
 348 current packet. The final panel shows how the trigger simulation reacted

⁴Very high speed integrated circuit Hardware Description Language

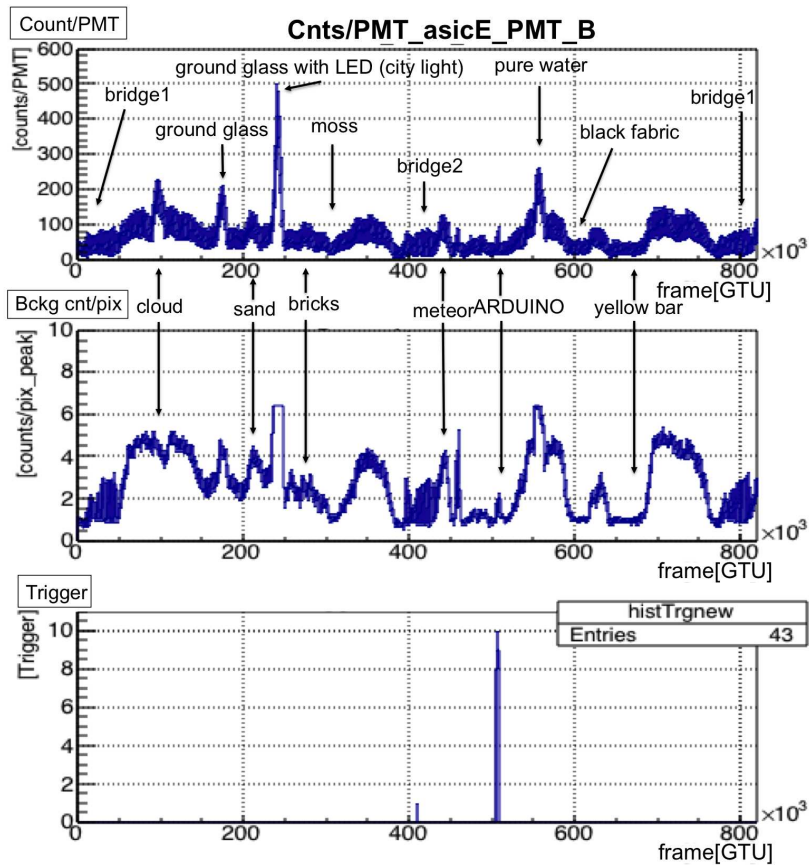


Figure 9: Reproduction of a full TurLab rotation with many types of light. Top plot shows the sum of the light collected by 1 MAPMT as a function of time. Middle plot shows the light intensity monitored by the pixel responsible to set the trigger thresholds of the MAPMT. Bottom plots show the triggered events. Except for two spurious cases due to quite variable background conditions (see middle panel) which could not be properly followed with the 50 ms dead time between packets, all the triggers coincide with the cosmic ray-like events generated by Arduino.

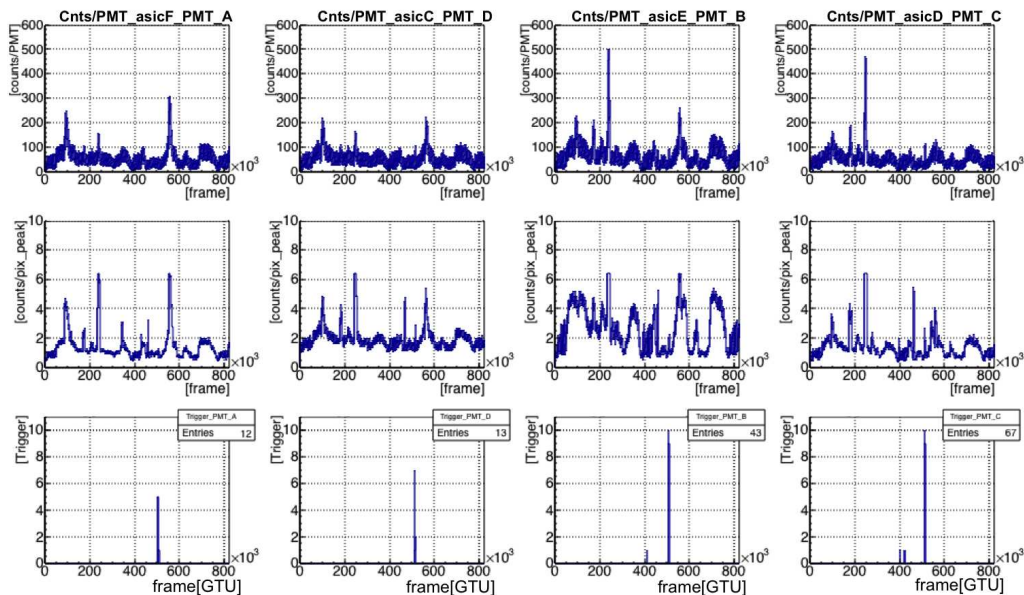


Figure 10: Reproduction of a full TurLab rotation with many types of light sources as shown in fig. 9 for the entire EC.

349 to this input. It shows when FLT's were issued based on signals in that
 350 MAPMT. Almost all triggers coincide with passing over the Arduino driven
 351 LED chain as it should be; the one that is not is due to a specific location
 352 near one of the two bridges crossing the tank where the variations of light
 353 reflection were still too fast to be compensated by the slower rotation of the
 354 tank. Fig. 10 shows top and bottom plots of Fig. 9 for all four MAPMTs. A
 355 similar response is obtained for all four MAPMTs all along the rotation.

356 To directly assess the impact of background on the FLT trigger scheme for
 357 EAS dedicated measurements were made at TurLab with the tank rotation
 358 stopped and the EC stationary above the Arduino driven white LED strip
 359 simulating EAS. Ambient light levels then controlled the background to the
 360 LED induced signal. These ambient light levels were varied between 0.1
 361 and 2.0 PE per pixel and per GTU, reflecting expectations for typical ISS
 362 observation background. The Arduino EAS were generated 1 ms apart in
 363 order to reduce the probability of recording such Arduino EAS in consecutive
 364 data packets, in which case the first EAS would set the background level for
 365 the second EAS. As the DAQ for EUSO@TurLab was not synchronized with
 366 track timing in the Arduino, extracting the packets containing a complete

367 Arduino track required some event selection.

368 This selection started from a 4×4 pixel box in that MAPMT which con-
 369 tained the brightest part of the Arduino LED simulated EAS. The stationary
 370 tank was oriented such that the Arduino LEDs were all within the field of
 371 view of a single MAPMT and the Arduino EAS were always crossing the
 372 same MAPMT pixels.

373 The LED sequence for these Arduino EAS was kept stable with ~ 30 PE
 374 at maximum, which corresponds to recording a $\sim 6 \times 10^{19}$ eV EAS in JEM-
 375 EUSO. A mask above the LEDs was used as an aperture to avoid unwanted
 376 reflections of LED light from nearby structures above the tank. The voltages
 377 supplied to the LEDs were also adjusted to dim the LEDs that were closer
 378 to the ends of the strip in an effort to provide a realistic EAS profile when
 379 the Arduino board sequentially lights up the LEDs in the strip.

380 If the PE count in the 4×4 pixel box smoothed over 5 GTUs exceeded
 381 the corresponding background estimate by more than 4σ , the data were con-
 382 sidered an Arduino EAS candidate. Such a candidate would subsequently
 383 be rejected if the excess occurred only in the first or last five GTUs of a 100
 384 GTU data packet, or if the preceding data packet also contained an Arduino
 EAS candidate. Fig. 11 shows PE counts for the relevant MAPMT over

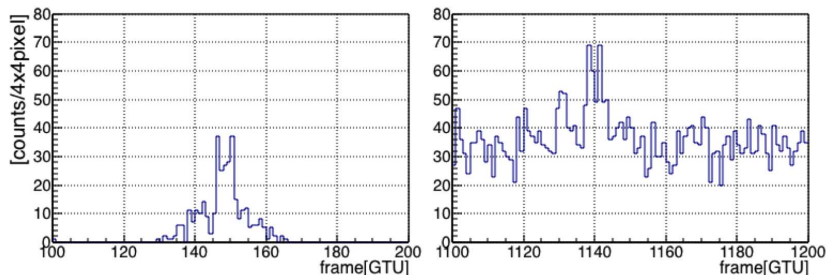


Figure 11: Example of light curves of two extracted Arduino events without background counts and with a background condition of ~ 2 counts GTU^{-1} pixel^{-1} , respectively.

385
 386 time in GTU units. The left panel shows a typical event produced by the
 387 LED strip without background. This highlights the event's original shape.
 388 The right one is a similar event produced under high background.

389 Events selected by this procedure were then fed into the VHDL trigger
 390 simulation. Table 2 shows that all the selected Arduino EAS also triggered
 391 in the FLT simulation. This together with the fact that when observing
 392 the rotating tank with its various implementations of atmospheric as well as

$N_{PEave./4\times 4pix}$	$N_{triggered}$	$N_{extracted}$
0.21	24	24
0.36	13	13
0.56	15	15
0.78	21	21
1.00	26	26
1.23	16	16
1.47	26	26
1.69	22	22
1.93	20	20
2.11	31	31

Table 2: Number of triggered and extracted cosmic-ray-like-track events in various background photon level conditions. $N_{PEave./4\times 4pix}$ indicates the average background level expressed in counts per pixel per GTU evaluated on a 4×4 pixel-box during the preceding packet of data, where no Arduino event was extracted.

393 ground-based light sources, albedo effects and generally varying background
394 light levels gave rise to only a few spurious triggers under very specific con-
395 ditions gives confidence that the current FLT implementation is ready for
396 deployment in JEM-EUSO.

397 4.2. Tests with EUSO-Balloon data

398 The EUSO-Balloon [20, 21] data taken during a 5 hour flight at 38 km
399 altitude in the vicinity of Timmins in Canada provides another testbed for
400 the FLT. Again the adequacy of the newly adopted background estimation
401 method with respect to keeping the trigger rate within the permissible bounds
402 in the presence of artificially and naturally encountered fluctuations in the
403 background lighting conditions as well as the FLT’s ability to trigger on
404 relevant optical phenomena was studied. While at TurLab the optics and
405 speed could be adjusted to match event duration and persistence in a pixel’s
406 FoV for the various phenomena recreated there, the EUSO-Balloon’s speed
407 and trajectory could not be controlled to that extent. On the other hand
408 EUSO-Balloon looked down on a real Earth environment just as JEM-EUSO
409 will, albeit from a much closer distance than the ISS. Thus were TurLab
410 strove to be realistic in an artificial environment, EUSO-Balloon was looking
411 at realistic settings compromising on perspective. Thus they each capture
412 different aspects of the challenges presented to an FLT operating at JEM-

413 EUSO.

414 In flight the EUSO-Balloon optics imaged a 60 km^2 surface area onto one
415 full PDM with its 9 ECs and a total of 36 MAPMTs. Just as at TurLab
416 the data acquisition did not allow to record data continuously, but took 128
417 GTU data packets at 18 Hz, translating into $320 \mu\text{s}$ of data recorded every
418 $\sim 55 \text{ ms}$. Data taking on the balloon was organized into runs. A new run
419 would be started after either 200 or 2000 data packets had been recorded.
420 In total about $4 \cdot 10^7$ GTUs were recorded with the camera looking down on
421 natural backgrounds like forests, lakes, and clouds, as well as city lights.
Fig. 12 traces the time variation of a typical one of the 2304 pixels in the

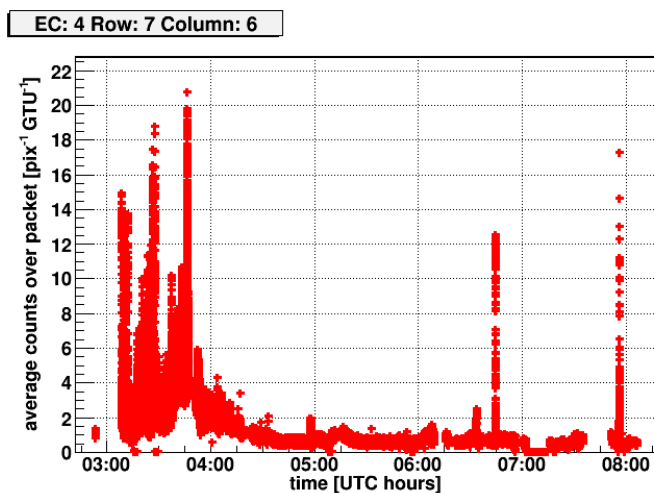


Figure 12: PE counts averaged over each recorded data packet for one typical pixel, covering the entire balloon flight.

422

423 camera. The city of Timmins for example crossed the field of view of that
424 pixel between 03:00 and 04:00 UTC. The low counts at the center of the data
425 taking period correspond to times when the balloon was passing over forests,
426 lakes, and clouds. The highest PE counts were recorded when the balloon
427 passed over an active mining operation.

428

429 For about two hours a helicopter was flying under the balloon. The
430 helicopter carried three different light sources: a UV LED, a Xe-Flashlamp
431 and a UV laser. This sources had the purpose of calibrating the detector
432 response and simulating EAS-like event patterns that in this paper are used
433 offline to test the FLT. Data analysis focused on about one hour of balloon
flight during which the helicopter was shooting underneath the balloon and

434 in the FoV of the camera. During this hour no other system tests interfered
435 with the measurements, and the flight path crossed over dark as well as bright
436 areas. This is essential to test the FLT logic under extreme conditions.

437 The data was divided into two data blocks: One block with so-called
438 “nominal” background levels as are expected for operation on the ISS with
439 ~ 0.6 PE/pixel/GTU averaged over a packet, and one block with a “high”
440 background of 5–10 PE/pixel/GTU average over a packet in some parts of
441 the FoV. This latter block of data was collected while passing over the mine
442 or a city. About 15% of MAPMT pixels that were not working properly were
443 excluded from the analysis.

444 The light sources on the helicopter were set up to emit signature patterns
445 that each served a distinct purpose [22]. First in the sequence was a UV-LED
446 (375 nm wavelength), the light output of which steadily increased with time
447 over 12 GTUs. From the balloon this signal appears as a stationary source
448 typically contained in a single MAPMT pixel. The UV-LED light output
449 was kept stable throughout the night and designed to raise the signal level
450 from ~ 1 to ~ 50 PE over the 12 GTUs in that pixel. This signal provides
451 a normalization for the distance between helicopter and EUSO-Balloon and
452 allows to determine an effective threshold for the FLT.

453 Next in the sequence was a laser pulse shot horizontally away from the
454 helicopter. This laser shot was fired about 25 GTU after the end of the
455 UV-LED signal, delivering ~ 5 mJ over 7.5 ns at a wavelength of 355 nm.
456 Depending on where in the balloon’s FoV the helicopter happened to be
457 at that time, it could take a maximum of 10 GTUs before the laser pulse
458 would leave the balloon’s FoV. The number of photons scattered out of such
459 a laser pulse roughly corresponds to the fluorescence light emitted at shower
460 maximum from a $\sim 10^{20}$ eV EAS [according to ESAF simulations](#) [23].

461 The balloon’s altitude being low compared to the ISS however meant that
462 the ~ 400 m \times 400 m of a 3×3 pixel cell on the ground was crossed by the
463 laser pulse in ~ 1 GTU, while the FLT is integrating over 5 GTU to establish
464 a threshold crossing. To retain the ability for the FLT to trigger, the last
465 light source in the sequence of light sources operated on the helicopter is a
466 xenon (Xe) discharge lamp (wavelength 337 nm) emitting its light over ~ 8
467 GTU, hereafter referred to as Xe flasher. This Xe flasher is triggered ~ 5 μ s
468 after the laser shot, and its light curve reaches its maximum three GTU from
469 its start, decreasing thereafter. This is reminiscent of the light curve along
470 EAS, and four different flash intensities were used to mimic different EAS
471 energies. A total helicopter light sequence therefore extends over ~ 50 GTU.

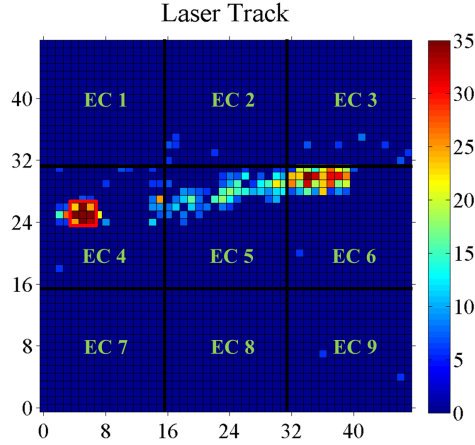


Figure 13: Image of a helicopter event obtained by integrating the counts in each pixel for the whole packet=1960 of RUN=043202 (128 GTUs). A threshold is applied to the minimum signal level to emphasise the location of the track. The UV-LED and Xe-flasher signals are centred around pixel at axis of abscissae $X=5$ and axis of ordinates $Y=25$.

472 Fig. 13 shows the integrated PE count per pixel for a 128 GTU data
 473 packet containing a whole helicopter light sequence. An offset was subtracted
 474 throughout to highlight the excess along the laser track. The helicopter with
 475 the UV-LED and the Xe flasher was in the pixel at $x=5$, $y=25$. The left panel
 476 of Fig. 14 shows the PE sum for each GTU in that same data packet for the
 477 3×3 pixel cell that is centered on the helicopter position at $x=5$, $y=25$. The
 478 UV-LED ramp can be seen to start from GTU 19. The laser shot is seen at
 479 GTU 55 and 56, and the Xe flash lamp is seen between GTU 58 and 65. The
 480 signal peaking at GTU 72 is attributed to an afterpulse in the Xe flasher.

481 Fig. 13 also identifies the ECs that the various signals appear in. For the
 482 UV-LED and the Xe flasher this is EC number 4, and the laser track starts
 483 in EC number 4 and then moves out through ECs 5 and 6. The right hand
 484 panel of Fig. 14 shows the number of ensuing FLT triggers per GTU for all
 485 ECs in that same data packet. The red line refers to triggers in EC number
 486 4, green to EC number 5, and blue to EC number 6. All signals are detected
 487 by the FLT algorithm, and the delay between the signal and trigger timings
 488 simply reflect the 5 GTU integration.

489 As the EUSO-Balloon DAQ and the helicopter light sequence each run
 490 on their own respective clocks and the DAQ recorded only $2.5 \times 128 = 320 \mu\text{s}$
 491 every ~ 55 ms ($\sim 0.6\%$), the vast majority of helicopter light sequences were

492 not recorded. There will also be events where only a part of the helicopter
493 light sequence overlapped with a DAQ data packet. Running the offline FLT
494 simulation through the data, 274 events were found in which at least two
495 ECs triggered the FLT algorithm.

496 Another peculiarity of EUSO-Balloon was that the optical module under
497 the balloon spun, constantly changing the FoV's alignment with respect to
498 both surface features and laser direction, and did so at a varying rate. This
499 meant that especially at the edges of the FoV stationary and other light
500 sources would often enter or exit the FoV during the ~ 55 ms dead time be-
501 tween data packets. This complication should clearly be more relevant where
502 stationary light sources on the ground play a significant role. As described
503 above, the data was sorted into two blocks: one with nominal and the other
504 with high background over locations lit up by human activity. The first block
505 contains a total [integrated time corresponding to](#) ~ 8.5 seconds, and the lat-
506 [ter corresponding to](#) ~ 6.5 seconds, with about one order of magnitude more
507 background light in this latter block's data on some parts of the FoV.

508 As expected the trigger rate under the more severe background conditions
509 is higher: In the high background block of data the FLT algorithm triggered
510 on 148 laser events and 59 others, while it triggered 126 laser and 17 other
511 events in the nominal background data block. Assuming all other events are
512 background, this puts the background rates for the current FLT trigger logic
513 at 2.0 Hz per 9 ECs for the nominal background data block and 9.1 Hz per
514 9 ECs for the high background data block. Under both conditions the rate
515 requirement of ~ 1 Hz per EC is met. In particular this means that despite
516 the particular challenge posed by the combination of balloon spinning and
517 DAQ deadtime the background estimation using the preceding data packet
518 works well.

519 The event shown in Fig. 13 and Fig. 14 and triggered on by the FLT
520 algorithm can be used to estimate an energy threshold for EAS that would
521 pass the FLT. Averaging over the seven lowest PE/GTU values that raise
522 trigger alerts in EC number 4 the average signal excess becomes 81 ± 13 and
523 the average background 39 ± 1 PE/GTU. This is a signal over background
524 ratio of 2.1 ± 0.3 for the 3×3 pixel cell raising the trigger. Comparing
525 this to ESAF simulations for EUSO-Balloon [23] under nominal background
526 conditions this ratio is reached for vertical EAS initiated by a $\sim 5 \times 10^{18}$ eV
527 proton. As the simulation also shows that showers at higher zenith angle
528 provide higher signal/GTU, this value should be considered an upper limit
529 for the energy threshold of FLT-triggered events recorded by EUSO-Balloon.

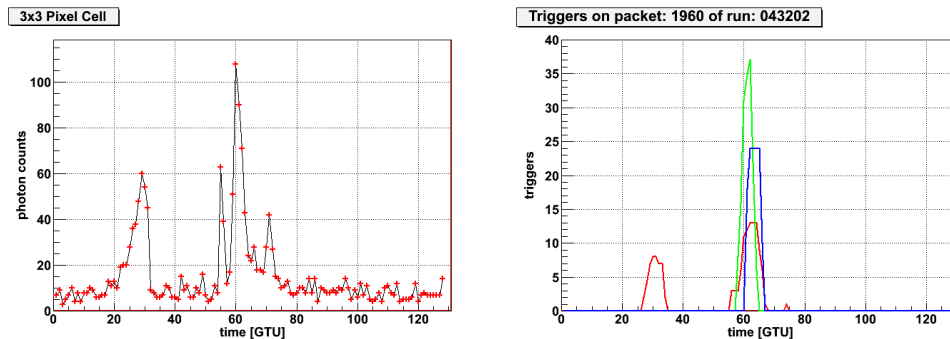


Figure 14: Left: Number of counts recorded in the 3×3 pixel-cell centred around $(X=5, Y=25)$ during the entire packet. See text for details. Right: Sequence of trigger alerts in the different ECs crossed by the laser track during the entire packet. See text for details.

530 Given its FoV and the measured CR rate at this energy this means that the
 531 FLT should trigger one event for every 24 hours of EUSO-Balloon livetime.

532 4.3. Tests with EUSO-TA data

533 TurLab measurements and EUSO-Balloon data were used to verify that
 534 the FLT and in particular its background estimation perform and meet the
 535 requirements under various realistic or even challenging background condi-
 536 tions. While comparing the lowest light level in EUSO-Balloon events that
 537 raised a FLT with simulation produced an estimate for the energy thresh-
 538 old in detecting cosmic ray particles, this is still a far cry from obtaining
 539 an efficiency curve for the FLT. This problem is addressed with data from
 540 EUSO-TA.

541 The EUSO-TA [18] telescope is a prototype of the JEM-EUSO space
 542 telescope with two 1 m^2 square Fresnel lenses. Just as for EUSO-Balloon its
 543 electronics comprise a full PDM with 9 ECs and 36 MAPMTs.

544 It is located right in front of the Black Rock Mesa (BRM) fluorescence
 545 detector (FD) site of the TA experiment in the Utah West Desert, USA [24].
 546 EUSO-TA's FoV of $11^\circ \times 11^\circ$ is contained within that of the BRM's FD and
 547 aligned such that it contains the vertical tracks from the pulsed 355 nm laser
 548 at TA's central laser facility (CLF). During TA data taking on the moonless
 549 parts of nights with amenable weather the CLF fires 300 vertical laser pulses
 550 of 3 mJ at 10 Hz every half hour. Providing atmospheric and calibration data
 551 for all three of TA's FD sites it is located centrally at an equal distance of
 552 21 km from each of the TA FDs, and therewith also 21 km from EUSO-TA.

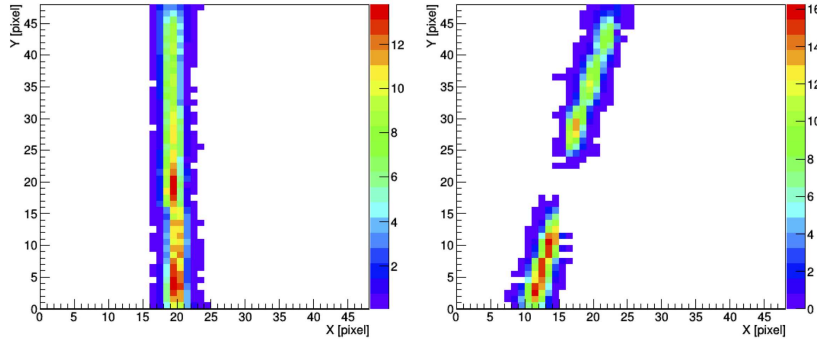


Figure 15: Left: an average of ~ 250 shots of CLF laser; right: an average of ~ 150 inclined shots of the Colorado School of Mines laser, located at 40 km from TA-EUSO, the missing part due to a non- functioning MAPMT in the center of the focal surface. The color scale on both pictures denotes the detector counts. Figure taken from [25].

553 Depending on the offset between GTU boundaries and laser shot, laser tracks
 554 took 6 to 8 GTUs for their image to cross the PDM at EUSO-TA. The left
 555 panel of Fig. 15 shows an average over ~ 250 such CLF shots as recorded by
 556 EUSO-TA.

557 The inclined laser track shown in the right panel of Fig. 15 is from a set
 558 of laser events produced with the help of a mobile UV laser belonging to the
 559 Colorado School of Mines. The missing piece in this laser track average was
 560 due to a defective MAPMT in EUSO-TA.

561 Also using a 355 nm laser the pulses from this mobile laser can be adjusted
 562 in intensity within a range of 1 to 86 mJ. As the laser itself is steerable, the
 563 geometry of the laser track can be varied more freely, and for the average
 564 over the ~ 150 laser pulses shown here the laser was shot at a distance of 40
 565 km with a pulse energy of 62 mJ.

566 Varying the laser pulse energies with this mobile laser at 34 km from
 567 EUSO-TA produced the trigger efficiency curve for the FLT that is shown
 568 in Fig. 16. As at these distances the laser pulses typically cross a few
 569 pixel/GTU, the FLT logic was adapted by setting $N_{pst} = 1$, while n_{thr}^{pix} and
 570 n_{thr}^{cell} were modified accordingly to keep the FLT trigger rates below the 1
 571 Hz/EC requirement. To determine the trigger efficiency, an external trig-
 572 ger, synchronized with the laser shooting, was supplied by the TA-FD to the
 573 EUSO-TA DAQ to always have the laser track inside a 128 GTU packet.
 574 The efficiency can then be determined by running the adapted FLT algo-

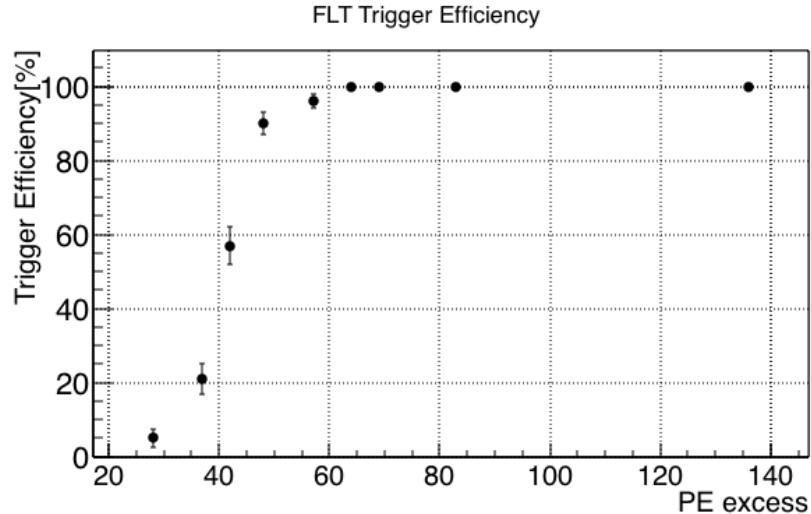


Figure 16: Trigger efficiency curve of FLT as a function of the signal excess recorded by TA-EUSO.

575 rithm over these data packets and counting the packets that raise an FLT.
 576 Laser pulse energies between 3 and 5 mJ were used for the first four points
 577 with signal excesses above background < 50 PE over all pixels in that GTU.
 578 Above 50 PE overall signal excess, which corresponds to ~ 25 PE in the rel-
 579 evant 3×3 pixel cell and 6 mJ pulse energy for this geometry, the trigger
 580 efficiency becomes 90% and higher. In a corresponding analysis for the 21 km
 581 CLF geometry the CLF's 3 mJ pulses were seen with 94% efficiency.

582 5. Conclusions

583 The FLT logic for use in JEM-EUSO as described above and implemented
 584 in VHDL was shown here a.) to work well in the presence of artificially
 585 produced as well as naturally encountered fluctuations in the background
 586 lighting conditions and b.) to keep the FLT rate within the permissible
 587 bounds while c.) being efficient at identifying event types with general EAS
 588 characteristics.

589 The FLT trigger as presented here is working at the MAPMT level and
 590 is based on the local persistency of a signal excess in a 3×3 pixel area,
 591 persisting a few GTUs. To achieve this an automatic evaluation of the average
 592 background level is derived from the preceding data package, as strategy that
 593 has proven successful even when individual data packages were separated by

594 up to a few hundred μs . Rejection for events with time duration too large
595 for an EAS signal, namely longer than 72 GTUs on the ISS, is also imple-
596 mented. This implementation for one EC requires only a few per cent of the
597 resources of commercial FPGAs, which allows to implement it within the
598 power constraints imposed on the ISS.

599 Tests performed with EUSO-Balloon and EUSO-TA data, as well as mea-
600 surements performed at the TurLab facility, allowed validating the main
601 functions of the algorithm. The system automatically adjusts the thresh-
602 olds to keep the rate of triggers on background fluctuations below 1 Hz/EC
603 even in the case of slow background variations. The FLT level trigger detects
604 EAS-like events with light intensities comparable to those JEM-EUSO would
605 observe in the energy range $E > 5 \cdot 10^{19}$ eV and in the presence of expected
606 night sky background. These results strenghten those obtained in [7] and
607 successive publications as they show that the trigger concept developed from
608 simulation can be effectively implemented in hardware and performs well on
609 real data.

610 The FLT has shown to be quite effective in rejecting city-like and other
611 slow but bright events such as meteors. Of the few spurious triggers that
612 occurred most were artefacts of discontinuities introduced by the available
613 equipment.

614 The examples shown in this paper are only a sub-sample of all tests
615 performed on the data reported here and the ongoing activities at the TurLab
616 facility and EUSO-TA.

617 The VHDL logic of the FLT is currently being implemented on the FPGA
618 of the PDM board. EUSO-SPB [26], the next stratospheric balloon flight, is
619 expected to host this trigger logic on-board to verify its performance on real
620 EAS.

621 **6. Acknowledgements**

622 This work was partially supported by the Basic Science Interdisciplinary
623 Research Projects of RIKEN and JSPS KAKENHI Grant (22340063, 23340081,
624 and 24244042), by the Italian Ministry of Foreign Affairs and International
625 Cooperation, by the 'Helmholtz Alliance for Astroparticle Physics HAP'
626 funded by the Initiative and Networking Fund of the Helmholtz Association,
627 Germany, and by Slovak Academy of Sciences MVTs JEM-EUSO as well as
628 VEGA grant agency project 2/0076/13. Russia is supported by the Russian
629 Foundation for Basic Research Grant No 13-02-12175-ofi-m. The Spanish

630 Consortium involved in the JEM-EUSO Space Mission is funded by MICINN
631 & MINECO under the Space Program projects: AYA2009-06037-E/AYA,
632 AYA-ESP2010-19082, AYA-ESP2011-29489-C03, AYA-ESP2012-39115-C03,
633 AYA-ESP2013-47816-C4, MINECO/FEDER-UNAH13-4E-2741, CSD2009-
634 00064 (Consolider MULTIDARK) and by Comunidad de Madrid (CAM) un-
635 der projects S2009/ESP-1496 & S2013/ICE-2822. The activities at TurLab
636 facility have been partially funded by the European High-Performance Infras-
637 tructures in Turbulence (EuHIT). The authors acknowledge strong support
638 from the French Space Agency CNES who provided - besides funding - the
639 leadership that made the EUSO-Balloon project possible in a very short time.
640 We are deeply indebted to the balloon division of CNES for a perfect launch,
641 smooth flight operation and flawless telemetry. The Canadian Space Agency
642 has provided outstanding facilities at the Timmins Stratospheric Balloon
643 Base, and a quick and careful recovery of the instrument. The authors dedi-
644 cate this paper to the memory of Dr. Jacek Karczmarczyk and Dr. Yoshiya
645 Kawasaki, who have contributed greatly to the project and will be deeply
646 missed.

647 **References**

- 648 [1] R. Benson and J. Linsley, Proc. 17th Int. Cosmic Ray Conf. (Paris),
649 (1981) 8.
- 650 [2] J.H. Adams et al. (JEM-EUSO Coll.), Exp. Astronomy 40 (2015) 3.
- 651 [3] F. Kajino et al. (JEM-EUSO Coll.), Nucl. Inst. Meth. A 623 (2010) 422.
- 652 [4] J.H. Adams et al. (JEM-EUSO Coll.), Exp. Astronomy 40 (2015) 19.
- 653 [5] M. Bertaina et al. (JEM-EUSO Coll.), Adv. Space Res. 53 (2014) 1515.
- 654 [6] C. Berat et al., Astrop. Phys. 33 (2010) 221.
- 655 [7] J.H. Adams Jr. et al. (JEM-EUSO Coll.), Astrop. Phys. 44 (2013) 76.
- 656 [8] M. Sato et al., Int. Journal of Mod. Phys. A 20/29 (2005) 6903.
- 657 [9] N. Sakaki et al., Proc. 30th Int. Cosmic Ray Conf. (Merida), HE 5 (2007)
658 1037.
- 659 [10] G.K. Garipov et al. (Tatiana Coll.), JETP Letters 4 (2005) 185.

- 660 [11] J. Bayer et al. (JEM-EUSO Coll.), Proc. 32th Int. Cosmic Ray Conf.
661 (Beijing), 3 (2011) 168; arXiv:1204.5065.
- 662 [12] J. Bayer et al. (JEM-EUSO Coll.), Proc. 33th Int. Cosmic Ray Conf.
663 (Rio de Janeiro), #0432 (2013); arXiv:1307.7071.
- 664 [13] M. Bertaina et al. (JEM-EUSO Coll.), Nucl. Instr. & Meth. A 824 (2016)
665 253.
- 666 [14] http://www.xilinx.com/support/documentation/data_sheets/ds150.pdf
- 667 [15] M. Bertaina et al. (JEM-EUSO Coll.), Exp. Astronomy 40 (2015) 117.
- 668 [16] J.H. Adams et al. (JEM-EUSO Coll.), Exp. Astronomy 40 (2015) 281.
- 669 [17] M. Bertaina et al. (JEM-EUSO Coll.), EPJ Web of Conferences 89
670 (2015) 03003.
- 671 [18] J.H. Adams et al. (JEM-EUSO Coll.), Exp. Astronomy 40 (2015) 301.
- 672 [19] <http://www.arduino.cc>
- 673 [20] P. von Ballmoos et al. (JEM-EUSO Coll.), Proc. 34th Int. Cosmic Ray
674 Conf. (Den Haag), #0725 (2015).
- 675 [21] M. Bertaina et al. (JEM-EUSO Coll.), Proc. 34th Int. Cosmic Ray Conf.
676 (Den Haag), #0890 (2015).
- 677 [22] J. Eser et al. (JEM-EUSO Coll.), Proc. 34th Int. Cosmic Ray Conf. (Den
678 Haag), #0860 (2015).
- 679 [23] F. Fenu et al. (JEM-EUSO Coll.), Proc. 34th Int. Cosmic Ray Conf.
680 (Den Haag), #0639 (2015).
- 681 [24] T. Abu-Zayyad, et al. (Telescope Array Coll.), Nucl. Instrum. Meth.
682 A689 (2012) 87.
- 683 [25] M. Casolino et al. (JEM-EUSO Coll.), Proc. 34th Int. Cosmic Ray Conf.
684 (Den Haag), #0636 (2015).
- 685 [26] L. Wiencke et al. (JEM-EUSO Coll.), Proc. 34th Int. Cosmic Ray Conf.
686 (Den Haag), #0165 (2015).